Acta Crystallographica Section B
**Structural Science**
ISSN 0108-7681

# Rationalizing the molecular origins of Ru- and Fe-based dyes for dye-sensitized solar cells

**Kian Sing Low,[a] Jacqueline M. Cole,[a,b,c]* Xiaolan Zhou[a] and Nataliya Yufa[a]**

[a]Cavendish Laboratory, University of Cambridge, J. J. Thomson Avenue, Cambridge CB3 0HE, England, [b]Department of Chemistry, University of New Brunswick, PO Box 4400, Fredericton, New Brunswick, Canada E3B 5A3, and [c]Department of Physics, University of New Brunswick, PO Box 4400, Fredericton, New Brunswick, Canada E3B 5A3

Correspondence e-mail: jmc61@cam.ac.uk

Received 6 October 2011
Accepted 1 March 2012

As part of an effort to design more efficient dyes for dye-sensitized solar cells (DSCs), structure–property relationships are established in the world's best-performing chemical series of dyes: 2,2′-bipyridyl-4,4′-carboxylatoruthenium(II) complexes. Statistical analysis, based on crystallographic data from the Cambridge Structural Database, is used to determine common structural features and the effects of structural change to its salient molecular constituents. Also included is the report of two new crystal structures for tris(2,2′-bipyridyl)dichlororuthenium(II)hexahydrate and tris(2,2′-bipyridyl)iron(II)dithiocyanate; these add to this statistical enquiry. Results show that the metal (*M*) core exhibits a distorted octahedral environment with $M$—N $\pi$-backbonding effects affording the propensity of the metal ion towards oxidation. The same characteristics are observed in iron-based analogues. The role of carboxylic groups in this series of dyes is assessed by comparing complexes which contain or are devoid of COOH groups. Space-group variation and large molecular conformational differences occur when COOH groups are present, while such structural features are very similar in their absence. The nature of the anion is also shown to influence the structure of COOH-containing complexes. These structural findings are corroborated by solution-based UV–vis absorption spectroscopy and DSC device performance tests. The presence of COOH groups in this series of compounds is shown to be mandatory for dye-uptake in $TiO_2$ in the DSC fabrication process. Throughout this study, results are compared with those of the world's most famous DSC dye, N3 (N719 in its fully protonated form): *cis*-bis(isothiocyanato)bis(2,2′-bipyridyl-4,4′-dicarboxylato)ruthenium(II). Overall, the molecular origins of charge-transfer in these complexes are ascertained. The findings have important implications to the materials discovery of more efficient dyes for DSC technology.

## 1. Introduction

The search for highly efficient light-sensitive dyes has been at the forefront of research in the field of dye-sensitized solar cells (DSCs) for more than a decade. This field arose from pioneering work by O'Regan and Grätzel, who showed that a nanocrystalline structured substrate could significantly enhance light absorption in a dye and thus produce significant solar cell efficiency (O'Regan & Grätzel, 1991). To date, ruthenium-based dyes have shown the best performance in a DSC, with the N3 dye *cis*-bis(thiocyanato)bis(2,2′-bipyridine-

4,4′-dicarboxylato)ruthenium(II) giving record efficiency of over 11% (Grätzel, 2005).[1] However, even with such results the cells incorporating ruthenium complexes are still struggling economically to compete with electricity produced from fossil fuels.

Concerning the metal core of these complexes, iron-based and copper-based dyes have been considered as an alternative photosensitizer for DSCs since they are much cheaper than analogous ruthenium-based dyes, albeit yielding reduced efficiency (Ferrere, 2002; Bessho *et al.*, 2008; Sakaki *et al.*, 2002). Meanwhile, it has been a long-held belief that a photosensitizer containing a carboxylate group is crucial to the performance of a DSC (Wang *et al.*, 2011; Grätzel, 2003). This provides effective binding and good electronic coupling to the nanocrystalline structured substrate. However, this is largely based on empirical evidence and there are few systematic studies that focus on justifying this hypothesis. Several groups have considered alternatives to carboxylate groups such as phosphonate groups (Park *et al.*, 2006). There is also evidence that other components of a molecule such as bipyridyl rings, which are common in the best performing dyes, have electronic interactions directly with the nanocrystalline structured substrate (Lee *et al.*, 2011). The bipyridyl ligand is ubiquitous in the best-performing ruthenium-based complexes, in part due to their good charge-transfer properties. Better charge transfer in these complexes provides an absorption spectrum that more closely matches that of the solar spectrum. The presence of more $\pi$-conjugation leads to an enhancement of intensity and bandwidth, allowing for the creation of more efficient solar cells.

Given that crystallography provides a quantitative description of $\pi$-conjugation *via* bond geometry, this paper seeks to locate the key patterns of $\pi$-conjugation in a family of bipyridyl-ligated ruthenium/iron complexes akin to N3. Furthermore, the paper seeks to address systematically the role of the carboxylate substituents on the bipyridine ligands. To this end, the molecular geometry of one iron complex and four ruthenium complexes, containing various carboxylate substituent levels, are compared statistically. These complexes are: tris(2,2′-bipyridyl)dichlororuthenium(II) hexahydrate (I); tris(2,2′-bipyridyl)iron(II)dithiocyanate (II); *cis*-bis(2,2′-bipyridyl)(2,2′-bipyridyl-4,4′-dicarboxylato)ruthenium(II) hexafluorophosphate (III) and tris(2,2′-bipyridyl-4,4′-dicarboxylato)ruthenium(II) dichloride (IV).

The crystal structures of (I) and (II) are presented in this paper in order to justify their structure–property relationships. In addition, the crystal structures are used as base motifs for a statistical analysis. These motifs [Fig. 1, (I) and (II)] were chosen firstly to test the effect of changing the transition metal atom and secondly to elucidate the effect of the carboxylate group on the bipyridyl delocalization. As mentioned before, and as has already been seen experimentally in the literature, there is an important contribution of the $\pi$-electron density in the pyridyl ring that is suggested to interact with the nanocrystalline (titanium dioxide, $TiO_2$) surface (Lee *et al.*, 2011). Furthermore, the NCS ligands in N3 have also been shown to interact with $TiO_2$ *via* spectroscopic techniques (O'Shea *et al.*, 2001). As we are interested in the effect of the carboxylate group on the bipyridyl rings and its interaction with the $TiO_2$, the chosen motifs (Fig. 1) contain no NCS ligands.

The Cambridge Structural Database (CSD; Allen, 2002) contains many reported crystal structures that have an identical cationic (main) molecular structure to that of either motif (I) or (II) in Fig. 1; only the associated counterion differs. This provides a useful basis set of structures from which to perform a statistical analysis. Furthermore, the CSD also has multiple structures whose pyridyl rings possess additional chemical substitution (excluding the bipyridyl bridge), which connects *via* a C atom. This permits further statistical analysis on how chemical substitution affects the delocalization of the pyridyl rings.

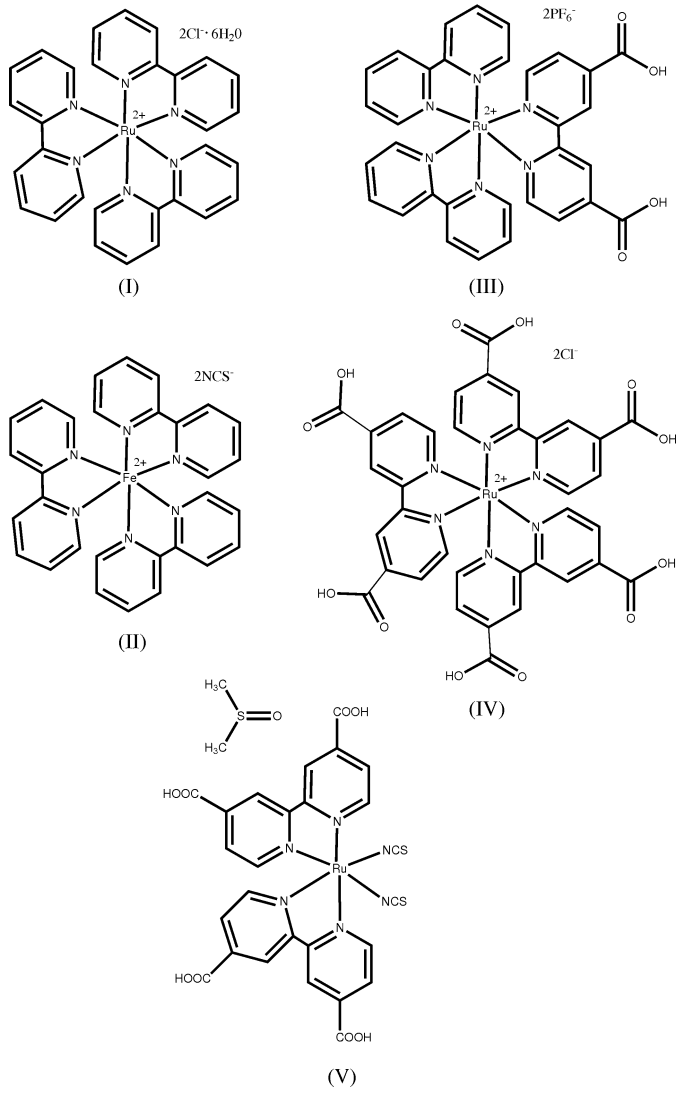


**Figure 1**
Complexes (I), (II), (III) and (IV), and N3 structural motifs (V).

[1] Since this paper submission, a report of a zinc porphyrin based dye has been published (Yella *et al.*, 2011) which breaks this world record, achieving 12% DSC performance efficiency.

Finally, with many different structures having identical cationic molecular structures and different counterions, we are able to assess the conformational similarity of the cationic parts to ascertain the effect of the counterion which has already been shown to be space-group sensitive (Caspar *et al.*, 2004; Pearson *et al.*, 2008).

## 2. Experimental

### 2.1. Crystallization, diffraction and spectroscopy

Complexes (II)–(IV) were purchased from Solaronix, while complex (I) was purchased from Sigma Aldrich. Originally in powder form, each complex was crystallized *via* slow solvent evaporation from methanol. Single crystals were mounted onto a Rigaku Saturn 724+ kappa CCD X-ray diffractometer, which is equipped with Mo $K\alpha$ radiation, SHINE Optics and an open-flow nitrogen Oxford Cryosystems CryostreamPlus.

UV–vis absorption spectra of all the complexes and N3 were recorded in water on a Hewlett Packard 8453 UV spectrophotometer.

**Table 1**
Experimental details for (I).

For all structures: hexagonal, *P6/mcc*, $Z = 4$. Experiments were carried out at 150 K with Mo $K\alpha$ radiation using a Rigaku Saturn724+ ($2 \times 2$ bin mode) diffractometer. Empirical absorption correction (using intensity measurements) in *CrystalClear* (Pflugrath, 1999). Refinement was on 57 parameters with 0 restraints. H-atom parameters were constrained.

| | (I) | (II) |
|---|---|---|
| Crystal data | | |
| Chemical formula | $C_{30}H_{24}N_6RuCl_2{\cdot}6H_2O$ | $C_{30}H_{24}FeN_6{\cdot}2NCS$ |
| $M_r$ | 748.62 | 642.28 |
| $a$, $c$ (Å) | 13.1383 (12), 20.995 (3) | 13.1837 (9), 21.2735 (14) |
| $V$ (Å3) | 3138.6 (6) | 3202.2 (4) |
| $F(000)$ | 1536 | 1216 |
| $D_x$ (Mg m$^{-3}$) | 1.584 | 1.213 |
| $\mu$ (mm$^{-1}$) | 0.72 | 0.20 |
| Crystal size (mm) | 0.21 × 0.16 × 0.12 | 0.18 × 0.12 × 0.10 |
| Data collection | | |
| $T_{min}$, $T_{max}$ | 0.676, 1.000 | 0.857, 1.000 |
| No. of measured, independent and observed [$I > 2\sigma(I)$] reflections | 11 174, 1220, 994 | 26 491, 1259, 1165 |
| $R_{int}$ | 0.086 | 0.043 |
| $\theta$ values (°) | $\theta_{max} = 27.5$, $\theta_{min} = 3.7$ | $\theta_{max} = 27.5$, $\theta_{min} = 3.6$ |
| $(\sin\theta/\lambda)_{max}$ (Å$^{-1}$) | 0.650 | 0.649 |
| Refinement | | |
| $R[F^2 > 2\sigma(F^2)]$, $wR(F^2)$, $S$ | 0.061, 0.153, 1.09 | 0.049, 0.115, 1.13 |
| No. of reflections | 1220 | 1259 |
| $\Delta\rho_{max}$, $\Delta\rho_{min}$ (e Å$^{-3}$) | 0.98, −0.56 | 0.32, −0.27 |

Computer programs: *CrystalClear* (Pflugrath, 1999), *SIR*92 (Altomare *et al.*, 1999), *SHELXS*97, *SHELXL*97, *SHELXTL* (Sheldrick, 2008), *WinGX* publication routines (Farrugia, 1999).

### 2.2. Dye-sensitized solar cell fabrication and characterization

Dye-sensitized solar cells were fabricated using Dyesol titanium dioxide ($TiO_2$) DSL 18NR-T paste. The titania was deposited onto cleaned fluorine-doped tin oxide (FTO) conductive glass (Solaronix S. A.) *via* the doctor blade method. These layers were then sucessively sintered for 10 min at 373 K, 10 min at 423 K, 30 min at 598 K, 5 min at 673 K and 30 min at 773 K and then allowed to cool to 343 K when it was dipped into a 0.5 m*M* dye solution using a 1:1 ratio of acetonitrile:*tert*-butanol solvent for N3 and 2,2,2-trifluoroethanol for (III) and (IV). The platinum counter electrode was prepared by spin-coating $H_2PtCl_6$ solution (52 m*M* in 2-propanol) onto the FTO-coated glass and then annealing at 723 K. The electrolyte used consisted of 50 m*M* iodide/triiodide in acetonitrile (Iodolyte AN-50 from Solaronix S. A.). The photoelectrode and counter electrode were sealed together using 25 µm Surlyn.

Current-voltage characteristics of the fabricated cells were measured under the equivalent of 100 mW cm$^{-2}$ AM 1.5 G illumination with a calibrated ABET Sun 2000 solar simulator, corrected for spectral mismatch.

### 2.3. Database study

Statistical analyses used the Cambridge Structural Database (CSD, Version 5.32, November 2010; Allen, 2002). *ConQuest*, Version 1.13 (Bruno *et al.*, 2002), was employed to search for structures that have a chemically identical cationic (main molecular) part of complex (I) and (II); there are many examples of these with different counterions.

Each search adhered to a few acceptance criteria for the structures found in the CSD:

(i) determined using single-crystal techniques (no powder diffraction structures);

(ii) having $R \leq 0.08$.

The only exception to this is the CSD entry for the N3 dye which has an $R$ factor of 0.0809 (Shklover *et al.*, 1997). This exception was permitted since this compound is still one of the best performing dyes even after a number of years. Additionally it is used across the world as a standard industrial reference dye.

The selected subsets of the CSD from the criteria above were statistically compared with their corresponding complex (I) or (II). The crystal packing feature in *Mercury* (CSD Version 2.4.5) was used to find the confomational differences between our investigated complexes and the *ConQuest* derived data sets (Weng, Motherwell *et al.*, 2008; Weng, Motherwell & Cole, 2008).

**Table 2**
N—$\widehat{\text{Ru}}$—N bite angles and the five closest structures to (I) out of a total of 43.

| Structure ID | Bite1 | Bite2 | Bite3 |
|---|---|---|---|
| Complex (I) | 79.0 (2) | 79.0 (2) | 79.0 (2) |
| KUFDOE[a] | 78.9 | 78.9 | 78.9 |
| GENCAE[b] | 79.1 | 79.1 | 79.1 |
| BPYRUF02[c] | 78.75 | 78.75 | 78.75 |
| GOLROO[d] | 78.79 | 78.79 | 78.79 |
| HIRDUH01[e] | 78.8 | 77.6 | 79.1 |
| N3[f] | 80 | 79.1 | – |

References: (*a*) Biner *et al.* (1992); (*b*) Pointillart *et al.* (2006); (*c*) Breu *et al.* (2000); (*d*) Pellaux *et al.* (1999); (*e*) Otsuka *et al.* (2001); (*f*) Shklover *et al.* (1997).

## 3. Results and discussion

Crystal data collection and refinement details for (I) and (II) are given in Table 1.[2] The corresponding crystal structures are illustrated in Figs. 2 and 3.

### 3.1. Database analysis

**3.1.1. *ConQuest*-derived subsets from the CSD**. There were also 43 structures in the CSD which had a chemically identical cationic (main molecular) part of complex (I) and that adhered to our acceptance criteria. This data set including complex (I) will subsequently be refered to as the set {Ru}.

We found that there were 33 structures in the CSD which had a chemically identical cationic (main molecular) part of complex (II) and that adhered to our acceptance criteria. This data set including complex (II) will subsequently be refered to as the set {Fe}.

Where these subsets are used, in the text that follows each relevant CSD entry will be refered to by its six letter unique identifier, as defined by the CSD; while the reference to the corresponding study will be cited alongside.

### 3.2. Metal environment

**3.2.1. Octohedral distortion in complexes (I) and (II)**. The bite angle between the bidentate ligands and the central metal atom is a key factor in determining the level of octahedral distortion in the complexes considered in this study. Given the multiple presence of bidentate bipyridyl ligands in (I), (II) and {Ru}, it could be deduced that the metal environment deviates significantly from regular octahedral symmetry. Table 2 lists the bite angles of the ruthenium complexes from {Ru} that are closest to that of (I).

As can be seen from Table 2, even though there is a significant octahedral distortion, this is a common aspect among structurally similar compounds in the CSD. The mean of the N—$\widehat{\text{Ru}}$—N bite angle in {Ru} is $\bar{x} = 78.8 \pm 0.5^\circ$. All but one of the structures found (XASZIB; Goforth *et al.*, 2005) lie within three standard deviations of this mean; XASZIB subtends an angle of 80.5 (5)° and removing this outlier yields an overall $\mu + 3\sigma = 80.2^\circ$.

[2] Supplementary data for this paper are available from the IUCr electronic archives (Reference: ZB5022). Services for accessing these data are described at the back of the journal.

Table 3 shows this similarity in bite angle of two similar temperature structures to complex (I). A similar bite-angle trend for similar temperature structures along with the same trend in Table 2 for different temperature structures provides evidence for this trend to be temperature-independent throughout {Ru}.

N3 does not have a third bipyridyl ring and thus no third bite angle. There the angle between the two (unidentate) NCS groups and the central ruthenium atom is 88.7 (5)°. Even so, Table 2 shows that there is good correlation of the first two bite angles between complex (I) and N3. It should be noted that a significant fraction of the N3 molecules, when adsorbed

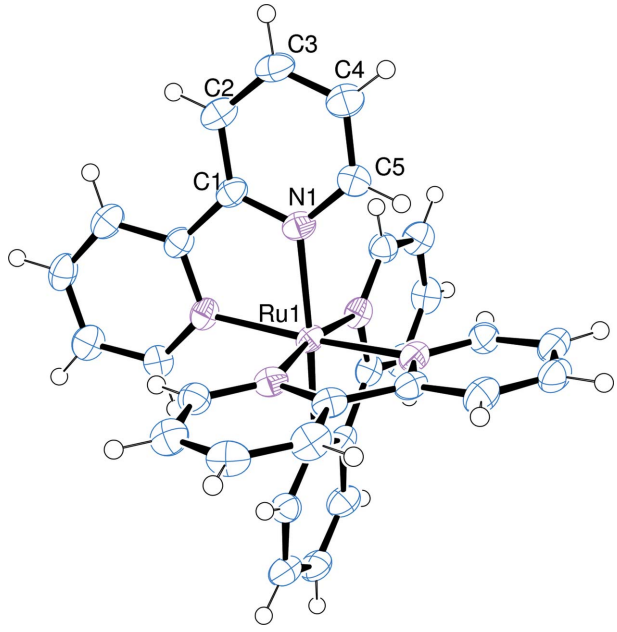


**Figure 2**
Molecular diagram of complex (I).

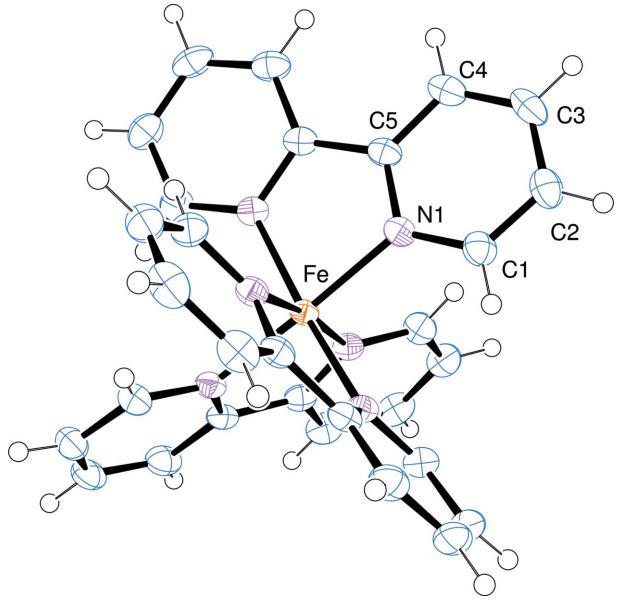


**Figure 3**
Molecular diagram of complex (II).

**Table 3**
N—$\widehat{\text{Ru}}$—N bite angles of TIWPEU (150 K; Meier *et al.*, 1997), PELSUV (153 K; Goforth *et al.*, 2006) and complex (I).

| Structure ID | Bite 1 | Bite 2 | Bite 3 |
|---|---|---|---|
| Complex (I) | 79.0 (2) | 79.0 (2) | 79.0 (2) |
| TIWPEU | 78.9 | 78.9 | 78.9 |
| TIWPEU | 79.8 | 79.8 | 79.8 |
| PELSUV | 79.3 | 78.8 | 78.9 |

on $TiO_2$, have one of the NCS groups interacting with the substrate (Johansson *et al.*, 2005). This adsorbed dye orientation along with the less distorted octahedral geometry around the NCS groups, which allows for better orbital overlap, may contribute to the superior efficiency of the N3 dye over that of other dyes without NCS groups.

Similar statistics were found for {Fe}; a mean bite angle of 81° exists. However, these values are slightly skewed due to two outliers [DOJKET (Li *et al.*, 2008) and OFONON (Wang *et al.*, 2008)] as these lie well outside a three standard deviation range from the mean. Without their consideration, $\bar{x} = 81.8 \pm 0.6°$.

**3.2.2. (Ru/Fe)—N bond lengths**. Average Ru—N and Fe—N bond lengths, where N belongs to a 2,2′-bipyridyl ligand, are 2.064 and 1.961 Å, according to the *International Tables for Crystallography* (ITC; Prince, 2004).

The {Ru} set of 43 structures in Fig. 4 contains a total of 366 Ru—N bonds with a mean of $\bar{x} = 2.058 \pm 0.015$ Å and only three bond lengths from three different structures lie outside the $3\sigma$ range.

Fig. 4 shows that 54% of all the bond lengths lie within the interquartile range (2.051–2.066 Å) with complex (I) Ru—N bond lengths [2.065 (3) Å] lying just inside this range. The Ru—N N3 bond lengths, pinpointed in Fig. 4, vary according to the two bidentate pipyridyl attachments: 2.01 (1) and 2.06 (1) Å in one bipyridyl ring, 2.03 (5) and 2.04 (2) Å in the other. Fig. 4 also shows that the Ru—N bonds in N3 are shorter in comparison to those in complex (I) and the ITC value. This reveals a resistance of N3 towards oxidation. Also, the shortest of these bond lengths in N3 are perpendicular to the NCS groups [see Fig. 1, (V)] and the longest ones *trans* to the NCS groups. This effect is attributed to $\pi$-backbonding between the Ru atom and the nitrogen of the NCS group. The $\pi$-backbonding increases the strength of this bond thus making it shorter; in turn, this weakens the *trans*-bipyridyl bond. The bonds perpendicular to the NCS groups are not as affected by the $\pi$-backbonding, thus making them stronger and shorter than those *trans* to the NCS group. The *trans* influence (Appelton *et al.*, 1973), which is the weakening of a metal–ligand bond owing to the strong influence of its *trans*-ligand, can also account for the two Ru—NCS bonds being among the longest in the structure. With the Ru—N (bipyridyl) bond having a stronger *trans* influence than Ru—NCS, this bond is shorter than the Ru—NCS bond. In contrast, where the *trans* ligands are both bipyridines the *trans* influence is equal; accordingly, so are their bond lengths.

These features bear strong parallels to the situation for (II). For {Fe}, the mean Fe—N bond length is $\bar{x} = 1.98 \pm 0.10$ Å for 270 bonds. This includes the two structures OFONON and DOJKET which again are both outliers for this data set. Without them $\bar{x} = 1.97 \pm 0.01$ Å and 55% of the bonds lie within the interquartile range (1.964–1.982 Å). However, both the ITC value and complex (II) bond lengths lie just outside of this range (see Fig. 5).

### 3.3. Bipyridyl ligand environment

**3.3.1. C—C bridging length in bipyridyl rings**. The C—C bonds bridging the two pyridyl fragments in all three complexes have a significant effect on the delocalization of the bipyridyl ligand in the structure. The C—C bridging bonds in complexes (I) [1.454 (9) Å] and (II) [1.460 (3) Å] are much

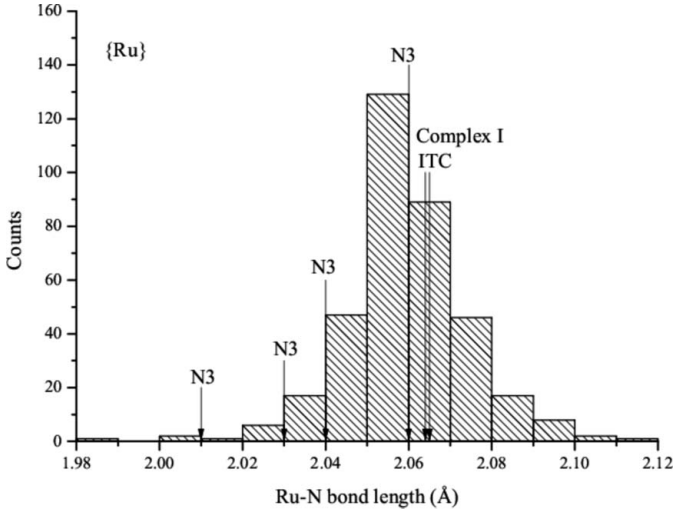


**Figure 4**
Histogram of {Ru} showing the distribution of the Ru—N bond length. Arrows mark the actual bond lengths of ITC, N3 and (I).

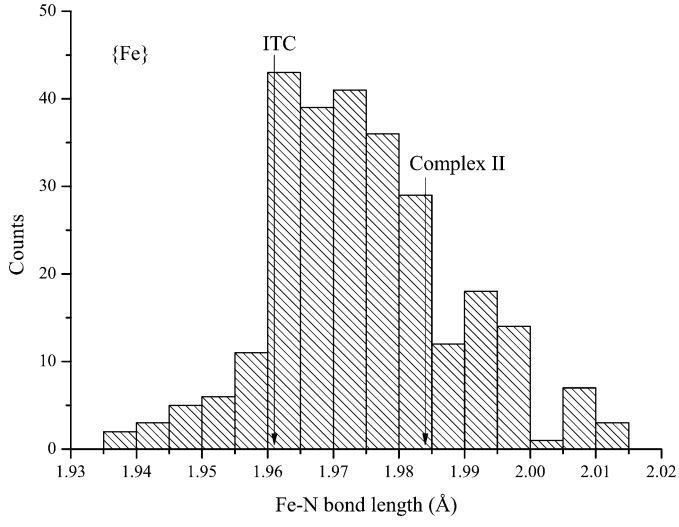


**Figure 5**
Histogram of {Fe} showing the distribution of Fe—N bond lengths excluding structures OFONON and DOJKET, and showing the positions of the ITC reference and (II).

shorter than one would expect, *cf.* the C—C bridging length of 1.490 (3) Å (Chisholm *et al.*, 1981) for 2,2′-bipyridine. This same trend of short C—C bonds is apparent in both {Ru} and {Fe}. Nonetheless, these bonds in (I) and (II) are shorter than the majority of similar structures in these two sets (see Figs. 6 and 7).

This shorter C—C bridge bond-length manifestation in (I), (II), {Fe} and {Ru} in part can be attributed to the bidentate attachment of the bipyridine to the Ru or Fe ion: the *M*—N coordination on each bipyridyl ring will pull on the C—C bridge in order to best accommodate the octahedral metal environment. $\pi\cdots\pi$ stacking is seen in the structure of 2,2′-bipyridine with a centroid–centroid distance of 3.87 Å between two partially overlapping pyridine rings (Chisholm *et al.*, 1981), although no such interactions are found in either complex (I) or (II). This could also contribute to the shorter C—C bridge bonds in complexes (I) and (II) compared with that of 2,2′-bipyridine.

While the temperature of the crystal structure determinations varied across the sets {Ru} and {Fe}, an analogous statistical analysis of room-temperature subsets of these data showed no observable difference. Thus, it is more instructive to use the larger statistically represented {Ru} and {Fe} sets.

Considering bipyridyl C—C bridging bonds more generally, their lengths closely resemble that of a C—C$sp^2$ single-bonded environment, *cf.* 1.487 Å for biphenyl rings, in contrast to 1.39 Å for a C⋯C delocalized bond, 1.32 Å for a C=C$sp^2$ double bond (Prince, 2004). This implies that the bipyridyl $\pi$-system does not extend between the two pyridine rings.

N3 has one C—C bridge length [1.45 (2) Å] that is similar to that in complex (I) [1.454 (9) Å] and one which is disparate [1.50 (2) Å]; the latter length is more comparable to the quoted ITC value.

The interpyridyl N—C—C—N torsion angle may also affect the average C—C bridging distance, and this is influenced by the level of planarity in the bipyridyl rings. In (I) and (II) the N—C—C—N torsion angle is −4.5 (6) and −5.0 (3)°. This compares with an average N—C—C—N angle of $\bar{x} = 4 \pm 3°$ for {Ru} and $\bar{x} = 5 \pm 4°$ for {Fe}. The standard deviations here reveal a significant range of twist angles in the statistical ensemble. This interpyridyl twist is likely to be another factor causing a short C—C bridging bond in this family of complexes as this reduces the bond stress otherwise created from having a small bite angle. This bipyridyl group twisting will also contribute to hindering the extension of the $\pi$-system between the two pyridyl fragments.

**3.3.2. Extent of aromaticity in the bipyridyl rings**. Complexes (I) and (II) each have three bipyridyl groups which are crystallographically equivalent. Indeed, the entire structure can be generated by the inherent space-group symmetry operations on a single pyridine ring, subject to either an Fe or Ru metal which is present in 1/6th occupancy according to the overall sixfold rotational symmetry. Furthermore, as shown in §3.3.1, there is no $\pi$-conjugation in the C—C bridge of the bipyridyl ligand. Thus, we can treat each half of the bipyridyl group as a single ring in our data analysis.

Based on molecular orbital theory, a pyridine ring should be aromatic (*i.e.* contains $4n + 2\pi$ electrons) and this should follow for the bipyridyl structure. According to the ITC, a pyridine ring has a N—C bond length of 1.337 Å and a C—C bond is 1.379 Å.

Figs. 8 and 9 display evidence for a slight deviation from aromatic bonding character in both complex (I) and (II) N—C bonds. Complex (I) has N—C bonds [1.345 (5) and 1.366 (5) Å] which are longer than the ITC value (Fig. 8). N3 also follows this trend with N—C bonds of 1.38 (2), 1.35 (2) Å for one half of the bipyridyl ring and 1.38 (2), 1.34 (2) Å for the other half of the bipyridyl ligand; correspondingly, the N—C bond pairs, 1.35 (2), 1.43 (7) and 1.29 (2), 1.34 (2) Å for the other bypyridine ring.

Complex (II) N—C bonds [1.364 (3) and 1.345 (3) Å] are significantly longer than the ITC value. These effects are

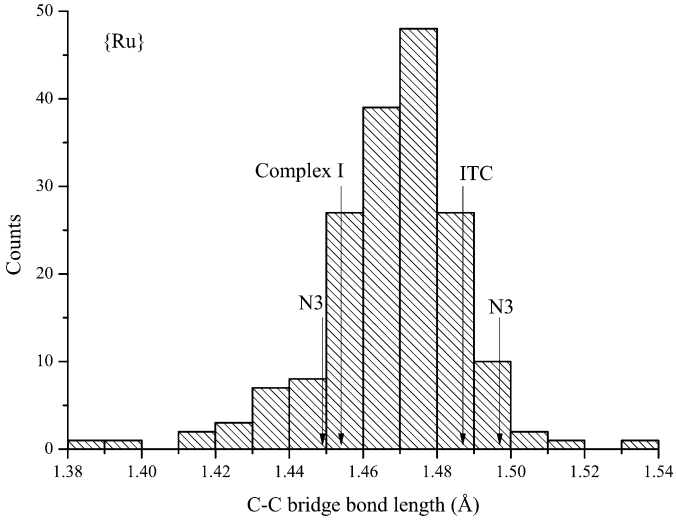


**Figure 6**
Histogram of {Ru} showing the distribution of the C—C bridge bond length.

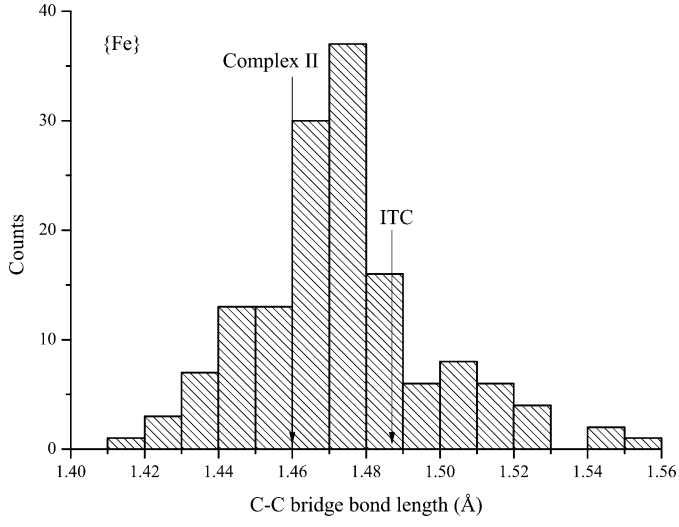


**Figure 7**
Histogram of {Fe} showing the distribution of the C—C bridge bond length.

mainly due to the metal–N coordination or the C—C bond substitution that bridges the other pyridine ring.

{Ru} has 720 N—C bonds with $\bar{x}$ = 1.35 ± 0.02 Å, while {Fe} contains 588 N—C bonds giving $\bar{x}$ = 1.35 ± 0.02 Å.

N—C bond lengths of the structures in {Ru} and {Fe} concur with the observed trend for (I) and (II): *i.e.* the majority of the bond lengths are longer than that expected for a delocalized pyridine bond (ITC value). 50% of the N—C bonds in {Ru} lie within the interquartile range (1.346–1.363 Å), but with the ITC value lying outside. Similarly 49% of the N—C bonds in {Fe} lie within the interquartile range (1.339–1.359 Å) which also does not contain the ITC value.

Considering the C=C (delocalized) bipyridyl bond lengths in {Ru} (1416 C=C bonds) and {Fe} (1152 C=C bonds), a similar fashion reveals a mean C=C pyridyl bond length, $\bar{x}$ = 1.38 ± 0.02 Å for both sets. Such bond lengths and those for complexes (I), (II) and N3 lie within one standard deviation of the aromatic ITC value.

**3.3.3. Bipyridyl ligand substitution effects**. The effect of *ortho*-, *meta*- and *para*-bipyridyl chemical substitution relative to the metal–N point of coordination was analysed. This required new sets to be constructed from the CSD which contain all structures that correspond to the same substructure search as for {Fe} and {Ru}, with the exception that an extra C atom is attached to either the *para*, *ortho* or *meta* position (Fig. 10).

As before we have labeled these as sets for ease of reference. {Ru-*ortho*}, {Ru-*meta*} and {Ru-*para*} contain 9, 27 and 31 suitable structures with 27, 71 and 126 bond lengths in their respective positions. {Fe-*meta*} contains 21 suitable structures; within these there are 123 bond lengths at the *meta* position. Analogous {Fe-*ortho*} and {Fe-*para*} sets were not analysed because only 1 and 0 structures respectively were located in the CSD.

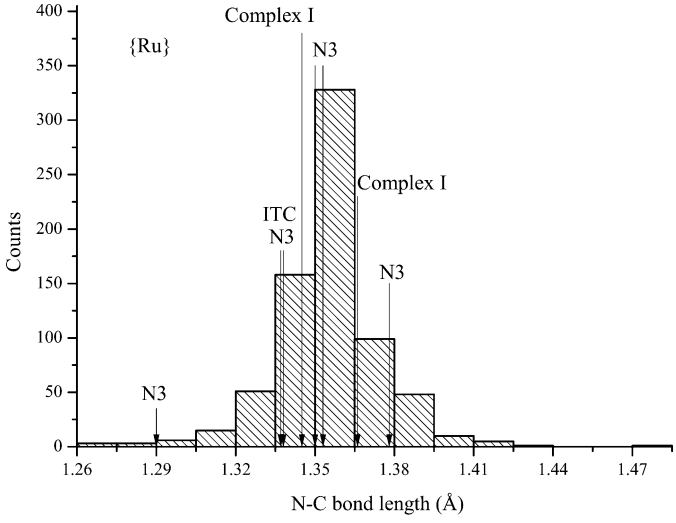


**Figure 8**
Histogram of {Ru} showing the distribution of the N—C bond length.

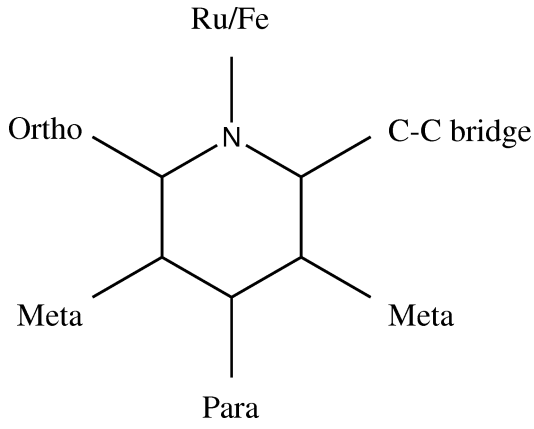


**Figure 10**
Diagram of bond labels in the pyridine ring.

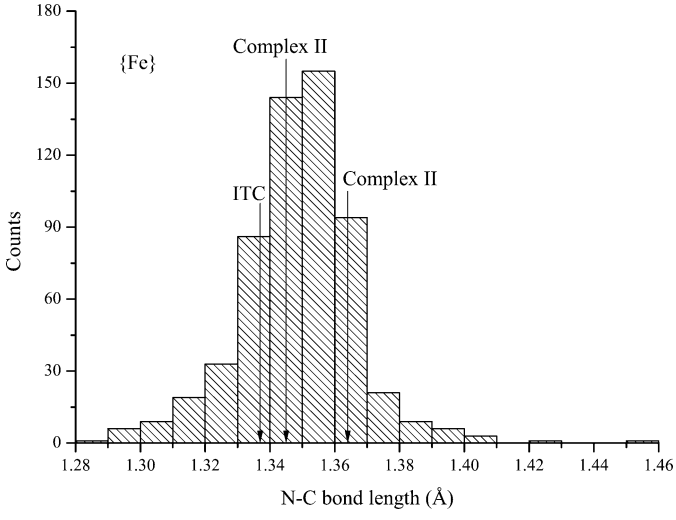


**Figure 9**
Histogram of {Fe} showing the distribution of the N—C bond length.

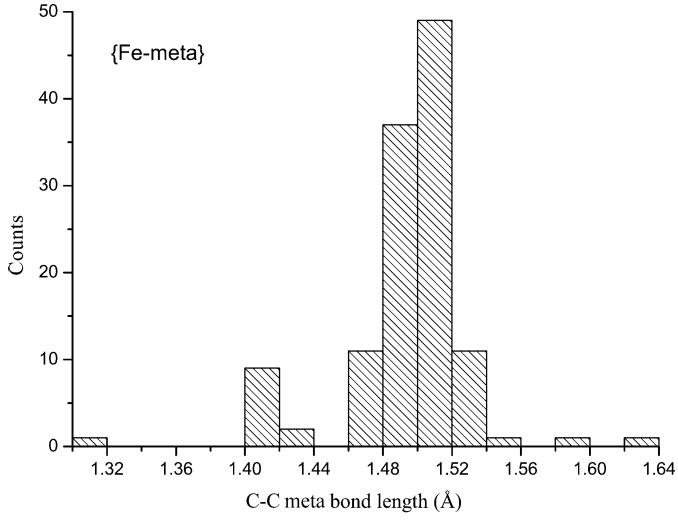


**Figure 11**
Histogram of the C—$C_{meta}$ bond lengths in {Fe-*meta*}.

In all sets, the bond lengths shorter than 1.100 Å were excluded as they were considered to be C—H bonds.

**3.3.4. C—C bond distributions for {Fe-*meta*}**. Fig. 11 shows that 54% of the C—$C_{meta}$ bonds in {Fe-*meta*} lie in the interquartile range (1.488–1.512 Å) with $\bar{x}$ = 1.49 ± 0.04 Å. These distances cover the range of single unconjugated $sp^2$—$C_{ar}$ to single $sp^3$—$C_{ar}$ bond hybridizations, given ITC values 1.488 and 1.513 Å. The variation between these values is attributed to the inductive effects of the *meta* substituents. There are outliers (1.62 and 1.305 Å) that both come from the same structure (NIYYEA; Pichon *et al.*, 2008), but from different moleules within the asymmetric unit.

**3.3.5. C—C and N—C bond distributions for {Ru-*ortho*}, {Ru-*meta*} and {Ru-*para*}**. 52% of C—$C_{ortho}$ bond lengths in {Ru-*ortho*} (Fig. 12) lie within the interquartile range (1.471–1.498 Å), where $\bar{x}$ = 1.48 ± 0.02 Å. This *ortho* substitution renders an elongated N—C bond relative to its expected ICT value and relative to that found in {Ru}; this is illustrated in Fig. 13.

For {Ru-*meta*}, the mean C—$C_{meta}$ bond length is $\bar{x}$ = 1.49 ± 0.02 Å with 52% of these lying in the interquartile range (1.482–1.509 Å, see Fig. 14). This is an identical 52% interquartile range distribution to {Ru-*ortho*}, but with a slight shift towards shorter C$sp^3$—$C_{ar}$-type bond lengths. The N—C bond lengths in {Ru-*meta*} have $\bar{x}$ = 1.35 ± 0.01 Å, which is the same as in {Ru}.

The C—$C_{para}$ interquartile range in {Ru-*para*} is 1.492–1.521 Å with 52% of bonds lying in this range and $\bar{x}$ = 1.50 ± 0.02 Å (Fig. 15). Once again, this bond-length distribution corresponds well to single C$sp^3$—$C_{ar}$ bonding. The N—C bond

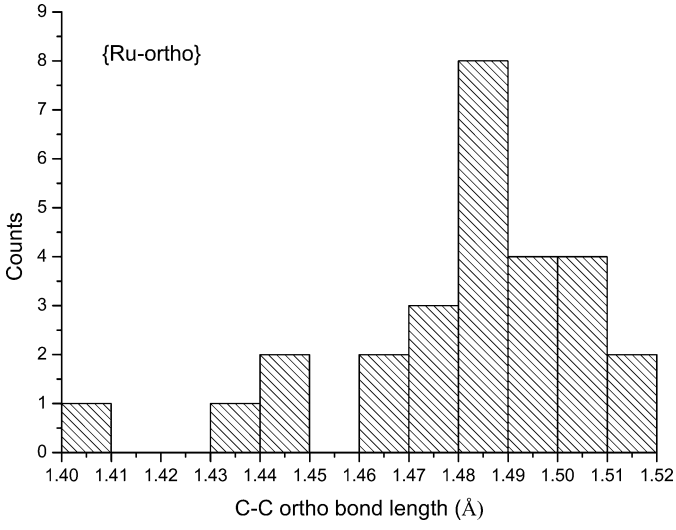


**Figure 12**
Histogram of C—$C_{ortho}$ bond lengths in {Ru-*ortho*}.

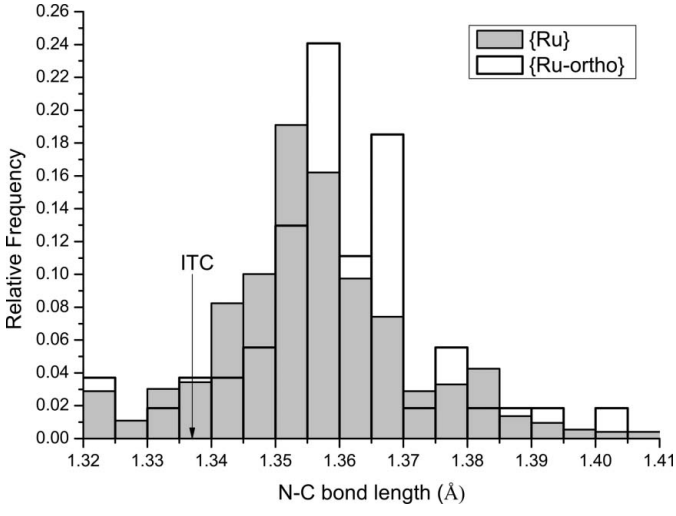


**Figure 13**
Histogram of N—C bond lengths in {Ru-*ortho*} and {Ru} and the ITC value shown.

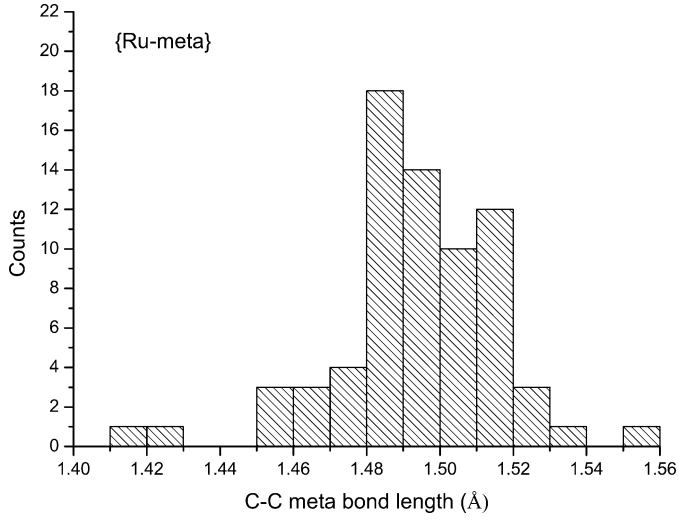


**Figure 14**
Histogram of C—$C_{meta}$ bond lengths in {Ru-*meta*}.

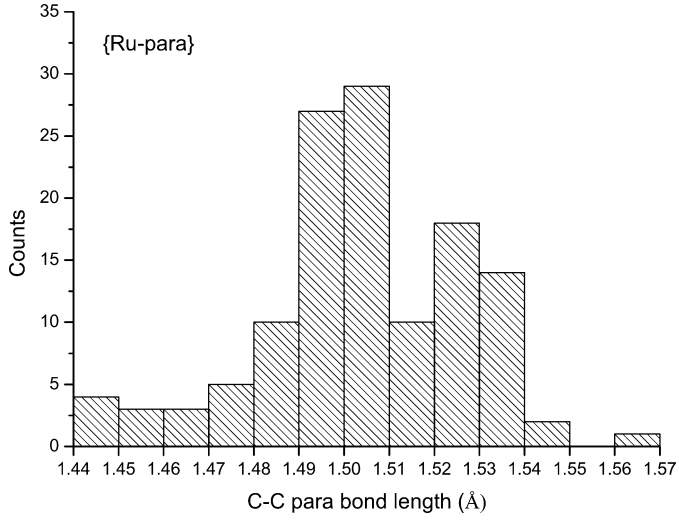


**Figure 15**
Histogram of C—$C_{para}$ bond lengths in {Ru-*para*}.

lengths in {Ru-*para*} also have the same mean ($\bar{x}$ = 1.35 ± 0.02 Å) as {Ru}.

### 3.4. The effect of the carboxylate group

Complexes (I), (III) and (IV) were compared to investigate the effect of the addition of a carboxylate group (COOH) on molecular structural changes, optical properties and solar cell efficiencies when used in a DSC. These three compounds were selected as they both have an identical cationic structure, except that the number of attached COOH groups may vary. This cation is a key consideration when relating the structure of the dye to its subsequent solar cell performance since dye sensitization of $TiO_2$ leaves a monolayer of only the dye cation (the anionic component of the dye is discarded *via* dissolution).

The difference in anchoring effects of carboxylate groups and phosphonate groups onto $TiO_2$ has already been investigated (Park *et al.*, 2006). It has also been reported that the most likely binding modes to $TiO_2$ originate from neighbouring bipyridyl ligands for structures similar to complex (IV). Furthermore, binding from two carboxylate groups in the same bipyridyl ligand is considered less favourable as in the case of (III) (Kilså *et al.*, 2004; Fillinger *et al.*, 2002; Nazeeruddin *et al.*, 2003).

Here we show that the carboxylate group in the dye structure not only improves the efficiency of a DSC but it is also essential for its operation.

**3.4.1. Structural variation**. Both (I) and (II) have different counterions and a different transition-metal central ion. However, they otherwise have a common cationic structure and this leads them to share the same space group. Accordingly, both (I) and (II) pack in a layered arrangement (Figs. 16 and 17). These two complexes do not possess a COOH group.

**Table 4**
The five closest structures to complex (I) from {Ru}.

| Structure ID | RMSD | Space group | Anion |
|---|---|---|---|
| Complex (I) | 0.000 | *P*6/*mcc* | $2Cl^-$, 6 $H_2O$ |
| KUFDOE | 0.080 | $R\bar{3}c$ | $3PF_6^-$ |
| GENCAE | 0.114 | $P4_332$ | $nC_6Mn_2O2_{12}^{2-}$, 0.25$nH_2O$ |
| BPYRUF02 | 0.116 | $P\bar{3}c1$ | $2PF_6^-$ |
| GOLROO | 0.118 | $P2_13$ | $nC_6NaO_{12}Rh_2^{2-}$ |
| HIRDUH01 | 0.120 | *C*2 | $C_6CrN_6^{3-}$, $Br^-$, $8H_2O$ |

In contrast, complex (III) does possess a COOH group and its cationic molecular structure may exist in one of at least three different space groups (Caspar *et al.*, 2004; Pearson *et al.*, 2008): *C*2, *C*2/*c* and *P*2(1)/*c*. Here, the anions are $7H_2O$ for *C*2, $2PF_6^-$ and $CH_3CN$ for *C*2/*c* and $3H_2O$ and $2PF_6^-$ for *P*2(1)/*c* structures; correspondingly, these crystallographic differences have been attributed to anionic variation. In turn, the sensitivity of space-group assignment, owing to the nature of the anion, has prospected that crystal field forces are important; this may imply that solvation effects are particularly sensitive in the solution state (Pearson *et al.*, 2008).

The conformational differences between our investigated complexes and the CSD subsets were investigated *via* the crystal packing feature in *Mercury* 2.4.5 (Weng, Motherwell *et al.*, 2008; Weng, Motherwell & Cole, 2008).

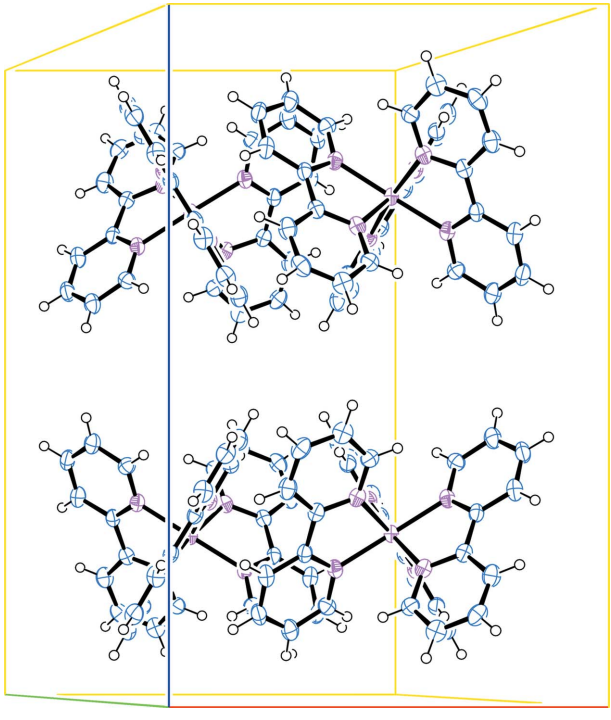

**Figure 16**
Crystal-packing diagram of (I). $H_2O$ molecules were omitted in this diagram *via* the SQUEEZE routine in *PLATON* (Spek, 2003).

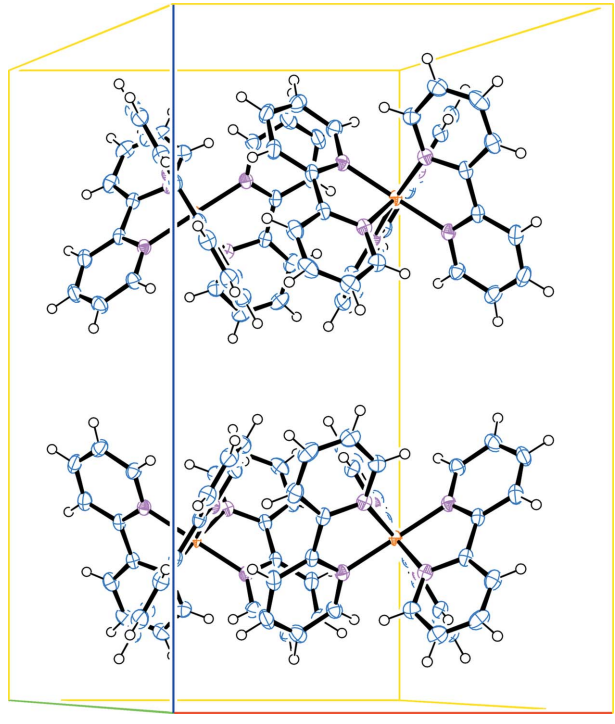

**Figure 17**
Crystal-packing diagram of (II). NCS anions were omitted in this diagram *via* the SQUEEZE routine in *PLATON* (Spek, 2003).

**Table 5**
Five closest structures to complex (II) from {Fe}.

| Structure ID | RMSD | Space group | Anion |
|---|---|---|---|
| Complex (II) | 0.000 | *P6/mcc* | $2NCS^{-}$ |
| JAMQIY | 0.091 | *C2/c* | $C_3HN_3S_3^{2-}$, $C_{10}H_8N_2$, $5.5H_2O$ |
| ISUDEF | 0.092 | *C2/c* | $O_{12}V_4^{4-}$, $10H_2O$ |
| LIPXIS | 0.096 | $P2_1/c$ | $C_6FeO_{12}^{4-}$, $12.25H_2O$ |
| NUZKOI | 0.118 | $P\bar{3}c1$ | $2PF_6^{-}$ |
| XIYCUE | 0.126 | $P2_12_12_1$ | $C_6NbO_{13}^{3-}$, $Cl^{-}$, $12H_2O$ |

**Table 6**
Conformational similarity of TIWPEU (150 K; Meier *et al.*, 1997) and PELSUV (153 K; Goforth *et al.*, 2006) structures to complex (II) from {Fe}.

| Structure ID | RMSD | Space group | Anion |
|---|---|---|---|
| Complex (I) | 0.000 | *P6/mcc* | $2Cl^{-}$, $6H_2O$ |
| TIWPEU | 0.189 | $P\bar{3}c1$ | None |
| PELSUV | 0.358 | $P\bar{1}$ | $n,n(Bi_3I_{11}^{2-})$ |

**Table 7**
Confromational similarity of PAHNUI (150 K; Parsons *et al.*, 2004) and WOBTIQ (150 K; Batten *et al.*, 2000) structures to complex (II) from {Fe}.

| Structure ID | RMSD | Space group | Anion |
|---|---|---|---|
| Complex (II) | 0.000 | *P6/mcc* | $2NCS^{-}$ |
| PAHNUI | 0.169 | $P2_1/c$ | $2B_1F_4^{1-}$, $3C_3H_7N_1O_1$ |
| WOBTIQ | 0.299 | *C2/c* | $2Cl_1O_4^{-}$ |

As can be seen from Tables 4 and 5 the root mean squared deviation (RMSD) between the cationic structure of (I) and (II) are low within the CSD subset chosen (see §2.3). This RMSD is a direct measure of the conformational difference between (I) or (II) and its similar structures in the CSD.

It is interesting to note that the conformational similarity of the cationic structure is good despite quite a variation in space group in both Tables 4 and 5. There is of course no COOH group present in these cations.

In order to ensure that a temperature-induced phase transition is not a possible cause for this space-group variation, cations of (I) and (II) were compared against crystallographic data collected at similar temperatures within their respective data sets (see Tables 6 and 7).

Even though a much larger RMSD value is observed in this comparison, relative to that of the five closest structures, the high conformational similarity of the cation is displayed (see Figs. 18 and 19). Therefore, it is reasonable to assume that a phase transition is not responsible for this space-group variation.

Complexes (III) and (IV) (Caspar *et al.*, 2004; Pearson *et al.*, 2008), however, show much greater conformational variation. The cation in (III) has three common structures to compare against each other, while that of complex (IV) (Eskelinen *et al.*, 2000) has only two. The RMSD values are 0.353 Å (SIXFUB to FEMGIO) and 0.437 Å (SIXFUB to QAGRIA) for (III) and 0.324 Å for (IV) when comparing all non-H atoms.

These conformational differences in (III) and (IV) further show the susceptibility of space-group variation of complexes due to counterion effects where COOH groups are present in the cation. In turn, this indicates the possiblity to exploit this susceptibility in order to structurally engineer dyes with a common cation to another but with different anions so as to effect better solvation and charge-transfer properties. Indeed, the cationic structure is the part of the dye that plays a key role in light absorption and charge transfer to the $TiO_2$ for DSC operation.

**3.4.2. UV–vis spectroscopy**. UV–vis absorption spectra were collected on all the investigated complexes, with water as the common solvent. Fig. 20 shows that the addition of the two COOH groups to (II) [to yield (III)] red-shifts the absorption and decreases the absorptivity of the dye. The peak absorption shifts from 451 to 457 nm. Where carboxylate groups exist on

**Figure 18**
Conformational similarity of (I) (black) and TIWPEU (yellow).

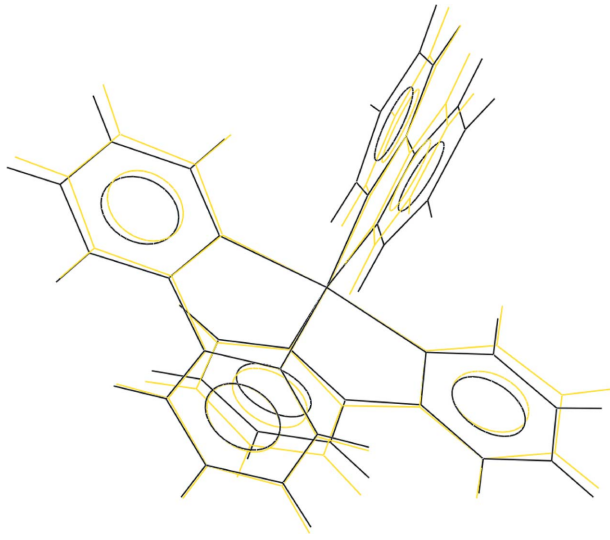

**Figure 19**
Conformational similarity of (II) (black) and PAHNUI (yellow).

all of the pyridyl rings [complex (IV)], the maximum absorption red-shifts further to 474 nm. The change of metal from Ru to Fe [(I) to (II)] affords a very different absorption profile. The peak absorption in complex (I) lies at 520 nm.

In all of these cases, the broad absorption peaks are due to metal-to-ligand charge transfer (MLCT), represented by a $d$–$\pi^*$ transition. The absorption spectra also show ligand-centred (LC) $\pi \rightarrow \pi^*$ transitions around 300 nm. These results are all generally consistent with previously published literature values (Kalyanasundaram, 1982; Nazeeruddin & Kalyanasundaram, 1989).

The MLCT broad bands in N3 are assigned to the peaks at 411 and 530 nm. The corresponding LC transition ($\sim$ 330 nm) is much more red-shifted than those of (I), (II), (III) or (IV).

**3.4.3. Solar cell efficiencies**. The role of the COOH group in the DSC operation has been described previously (Park *et al.*, 2006; De Angelis *et al.*, 2007). Here we show how not only is the COOH group critical for ultrafast charge injection from the dye to the $TiO_2$, but it is also essential for dye uptake onto $TiO_2$ and consequent solar cell functionality. All solar cells in this study were fabricated in one batch to ensure consistency in operational performance. Moreover, half the cells were sensitized with (I), (II), (III) or (IV), while the other half were sensitized with N3.

Table 8 shows that cells made with complexes (I) and (II) afforded negligible DSC efficiency. This result owes itself to the lack of dye adsorption onto the $TiO_2$ as could be seen by visual inspection (Figs. 23 and 22). This lack of dye absorption is attributed to the absence of any carboxylate group in these complexes which would otherwise act as a dye anchoring group to $TiO_2$.

Contrast the lack of colouration of the $TiO_2$ layer in the Ru-based complex (II) (Fig. 22) against that of a DSC which contains a Ru-based dye with COOH groups [complex (III)]: this gives a light orange colour to the sensitized $TiO_2$ layer (Fig. 23) and a significant DSC efficiency, as showed by the IV curve in Fig. 21 and the summary in Table 8.

**Table 8**
DSC efficiencies with N3 dye and complexes (I)–(IV).

$V_{oc}$ is the open circuit voltage, $J_{sc}$ is the short circuit current density, fill factor = max power point/$V_{oc} * I_{sc}$ ($I_{sc}$ = short circuit current) and efficiency = max power point/(1000 W m$^{-2}$ * cell active area).

| Sensitizer | $V_{oc}$ (V) | $J_{sc}$ (mA cm$^{-2}$) | Fill factor | Efficiency (%) |
|---|---|---|---|---|
| N3 | 0.61 | 19.38 | 0.68 | 6.28 |
| Complex (I) | 0.28 | 0.07 | 0.43 | 0.01 |
| Complex (II) | 0.45 | 0.56 | 0.50 | 0.13 |
| Complex (III) | 0.43 | 7.53 | 0.67 | 0.95 |
| Complex (IV) | 0.60 | 7.53 | 0.69 | 1.96 |

## 4. Concluding remarks

Concerted crystal structure analyses, UV–vis absorption spectroscopy and DSC device performance tests on five strategically related dyes have been performed. This has afforded new insights into structure–property relationships in a family of dyes for DSC technology. Understanding the molecular origins of dye functionality in currently leading dye families is very important for future material discovery efforts that aim to realise more efficient dyes for DSCs *via* quantum-tailored design. Our results not only demonstrate the type of 'molecular lego' that is needed to build new molecular dyes, but they also show charge-transfer characteristics which need to be controlled within the whole device design in order to yield optimum DSC performance. See, for example, the propensity of a metal ion towards oxidation, the requirements of the $TiO_2$ anchoring group (COOH in this study), and the effect of molecular charge transfer in the DSC electron injection process. Supramolecular crystal structure considerations also imply a sensitivity of certain dyes towards solvation and dye aggregation effects. While the cationic part of the dye is the predominant component featured in the DSC device, we show that the nature of the anion could nevertheless be exploited in

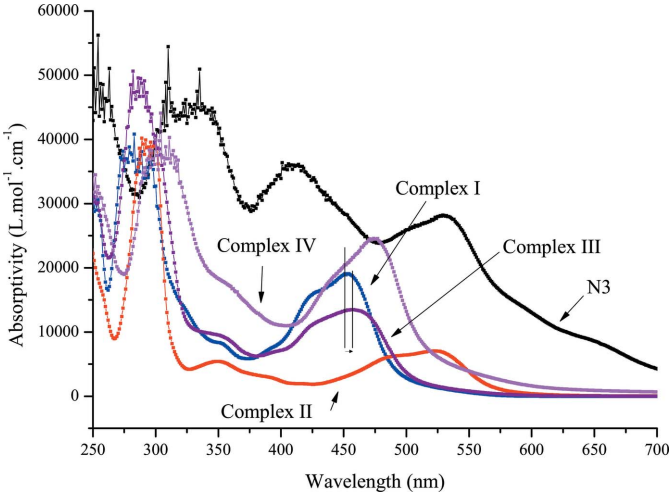


**Figure 20**
UV–vis spectra of the four complexes and N3 in water.

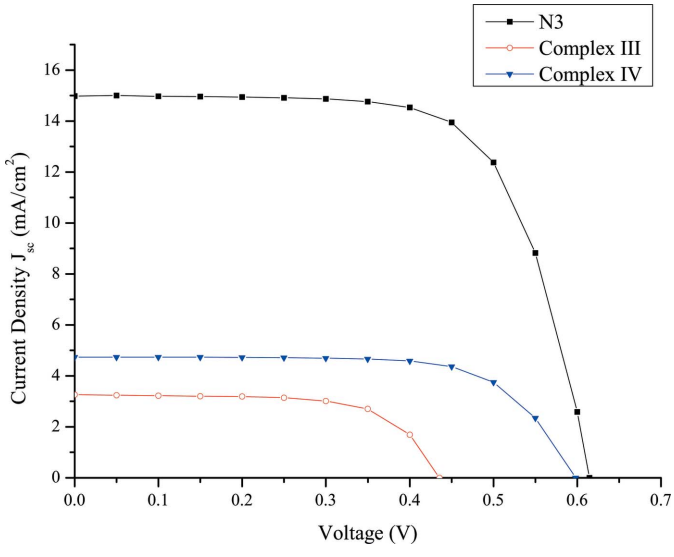


**Figure 21**
UV curves of the best perfoming cells made with N3, complexes (III) and (IV).

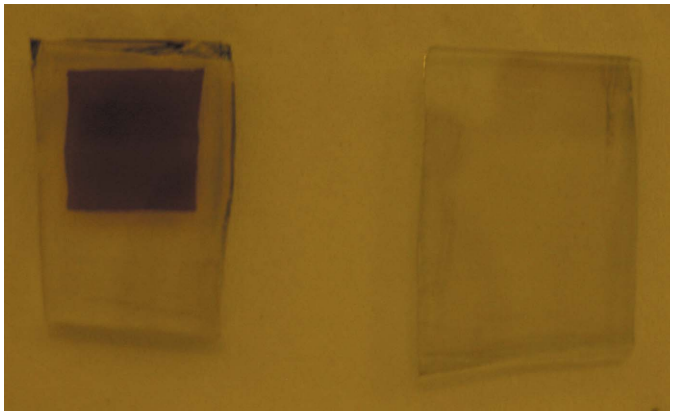

**Figure 22**
N3 (left) and (II) (right) electrodes after 12 h of dye sensitization.

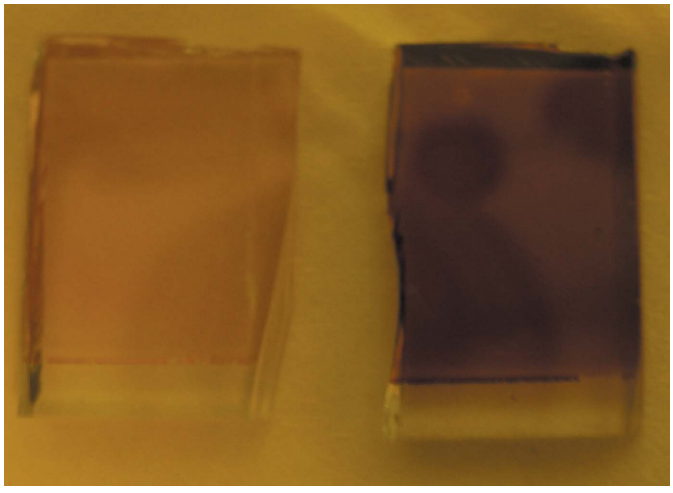

**Figure 23**
Complex (III) (left) and N3 (right) electrodes after 12 h of dye sensitization.

the future design of new dyes. The fact that this study focuses on such a high-profile family of subject materials (relating to N3) is particularly pertinent to the overall objective of smart material design of new classes of dyes for DSC technology.

KSL wishes to thank the EPSRC for funding (Grant No. EP/P504120/1). JMC is indebted to the Royal Society for a University Research Fellowship and the University of New Brunswick for the UNB Vice-Chancellor's Research Chair.

## References

Allen, F. H. (2002). *Acta Cryst.* B**58**, 380–388.
Altomare, A., Burla, M. C., Camalli, M., Cascarano, G. L., Giacovazzo, C., Guagliardi, A., Moliterni, A. G. G., Polidori, G. & Spagna, R. (1999). *J. Appl. Cryst.* **32**, 115–119.
Appelton, T. G., Clark, H. C. & Manzer, L. E. (1973). *Coord. Chem. Rev.* **10**, 335–422.
Batten, S. R., Murray, K. S. & Sinclair, N. J. (2000). *Acta Cryst.* C**56**, e320.
Bessho, T., Constable, E. C., Graetzel, M., Hernandez Redondo, A., Housecroft, C. E., Kylberg, W., Nazeeruddin, M. K., Neuburger, M. & Schaffner, S. (2008). *Chem. Commun.* **32**, 3717–3719.
Biner, M., Buergi, H. B., Ludi, A. & Roehr, C. (1992). *J. Am. Chem. Soc.* **114**, 5197–5203.
Breu, J., Domel, H. & Stoll, A. (2000). *Eur. J. Inorg. Chem.* **2**, 2401–2408.
Bruno, I. J., Cole, J. C., Edgington, P. R., Kessler, M., Macrae, C. F., McCabe, P., Pearson, J. & Taylor, R. (2002). *Acta Cryst.* B**58**, 389–397.
Caspar, R., Musatkina, L., Tatosyan, A., Amouri, H., Gruselle, M., Guyard-Duhayon, C., Duval, R. & Cordier, C. (2004). *Inorg. Chem.* **43**, 7986–7993.
Chisholm, M. H., Huffman, C., Rothwell, I. P., Bradley, P. G., Kress, N. & Woodruff, W. H. (1981). *J. Am. Chem. Soc.* **103**, 4945–4947.
De Angelis, F., Fantacci, S., Selloni, A., Grätzel, M. & Nazeeruddin, M. K. (2007). *Nano Lett.* **7**, 3189–3195.
Eskelinen, E., Luukkanen, S., Haukka, M., Ahlgrén, M. & Pakkanen, T. A. (2000). *J. Chem. Soc. Dalton Trans.* pp. 2745–2752.
Farrugia, L. J. (1999). *J. Appl. Cryst.* **32**, 837–838.
Ferrere, S. (2002). *Inorg. Chim. Acta*, **329**, 79–92.
Fillinger, A., Soltz, D. & Parkinson, B. A. (2002). *J. Electrochem. Soc.* **149**, A1146.
Goforth, A. M., Gardinier, J. R., Smith, M. D., Peterson Jr, L. & zur Loye, H.-C. (2005). *Inorg. Chem. Commun.* **8**, 684–688.
Goforth, A. M., Tershansy, M. A., Smith, M. D., Peterson Jr, L. & Loye, H.-C. zur (2006). *Acta Cryst.* C**62**, m381–m385.
Grätzel, M. (2003). *J. Photochem. Photobiol. Chem.* **4**, 145–153.
Grätzel, M. (2005). *Inorg. Chem.* **44**, 6841–6851.
Johansson, E. M. J., Hedlund, M., Siegbahn, H. & Rensmo, H. (2005). *J. Phys. Chem. B*, **109**, 22256–22263.
Kalyanasundaram, K. (1982). *Coord. Chem. Rev.* **46**, 159–244.
Kilså, K., Mayo, E. I., Brunschwig, B. S., Gray, H. B., Lewis, N. S. & Winkler, J. R. (2004). *J. Phys. Chem. B*, **108**, 15640–15651.
Lee, K. E., Gomez, M. A., Regier, T., Hu, Y. & Demopoulos, G. P. (2011). *J. Phys. Chem. C*, pp. 5692–5707.
Li, M., Niu, H. & Wang, W. (2008). *Z. Naturforsch.* **2**, 183–186.
Meier, R. P. K. K., Pettman, R. B., Soc, J. A. C., Senge, M., Gerzevske, K. R., Vicente, M. G. H., Perez-Cordero, E. E., Campana, C. & Echegoyen, L. (1997). *Angew. Chem. Int. Ed. Engl.* pp. 137–140.
Nazeeruddin, M. K., Humphry-Baker, R., Liska, P. & Grätzel, M. (2003). *J. Phys. Chem. B*, **107**, 8981–8987.
Nazeeruddin, M. K. & Kalyanasundaram, K. (1989). *Inorg. Chem.* **28**, 4251–4259.
O'Regan, B. & Grätzel, M. (1991). *Nature*, **97**, 1102–1111.
O'Shea, J. N., Schnadt, J., Brühwiler, P. A., Hillesheimer, H., Mårtensson, N., Patthey, L., Krempasky, J., Wang, C., Luo, Y. & Ågren, H. (2001). *J. Phys. Chem. B*, **105**, 1917–1920.
Otsuka, T., Sekine, A., Fujigasaki, N., Ohashi, Y. & Kaizu, Y. (2001). *Inorg. Chem.* **40**, 3406–3412.
Park, H., Bae, E., Lee, J.-J., Park, J. & Choi, W. (2006). *J. Phys. Chem. B*, **110**, 8740–8749.
Parsons, S., Usher, P., Yellowlees, L. & Wood, P. (2004). Personal communication.
Pearson, P., Bond, A. M., Deacon, G. B., Forsyth, C. & Spiccia, L. (2008). *Inorg. Chim. Acta*, **361**, 601–612.
Pellaux, R., Decurtins, S. & Schmalle, H. W. (1999). *Acta Cryst.* C**55**, 1075–1079.
Pflugrath, J. W. (1999). *Acta Cryst.* D**55**, 1718–1725.
Pichon, C., Dolbecq, A., Mialane, P., Marrot, J., Rivière, E., Goral, M., Zynek, M., McCormac, T., Borshch, S. A., Zueva, E. & Sécheresse, F. (2008). *Chem. Eur. J.* **14**, 3189–3199.
Pointillart, F., Train, C., Boubekeur, K., Gruselle, M. & Verdaguer, M. (2006). *Tetrahedron Asymmetry*, **17**, 1937–1943.
Prince, E. (2004). *International Tables for Crystallography*, Vol. C. Dordrecht: Kluwer Academic Publishers.

Sakaki, S., Kuroki, T. & Hamada, T. (2002). *J. Chem. Soc. Dalton Trans.* p. 840.
Sheldrick, G. M. (2008). *Acta Cryst.* A**64**, 112–122.
Shklover, V., Nazeeruddin, M.-K., Zakeeruddin, S. M., Barbé, C., Kay, A., Haibach, T., Steurer, W., Hermann, R., Nissen, H.-U. & Grätzel, M. (1997). *Chem. Mater.* **9**, 430–439.
Spek, A. L. (2003). *J. Appl. Cryst.* **36**, 7–13.
Wang, J., Bai, F.-Q., Xia, B.-H., Feng, L., Zhang, H.-X. & Pan, Q.-J. (2011). *Phys. Chem. Chem. Phys.* **13**, 2206–2213.
Wang, J.-P., Guo, G.-L. & Niu, J.-Y. (2008). *J. Mol. Struct.* **885**, 161–167.
Weng, Z. F., Motherwell, W. D. S., Allen, F. H. & Cole, J. M. (2008). *Acta Cryst.* B**64**, 348–362.
Weng, Z. F., Motherwell, W. D. S. & Cole, J. M. (2008). *J. Appl. Cryst.* **41**, 955–957.
Yella, A., Lee, H.-W., Tsao, H. N., Yi, C., Chandiran, A. K., Nazeeruddin, M. K., Diau, E. W.-G., Yeh, C.-Y., Zakeeruddin, S. M. & Gratzel, M. (2011). *Science*, **334**, 629–633.